Crystallographic Refinement by Simulated Annealing: Methods and Applications

Axel T. Brunger and Luke M. Rice

The Howard Hughes Medical Institute and
Department of Molecular Biophysics and Biochemistry,
Yale University,
New Haven, CT 06520
phone: (203) 432-6143
FAX: (203) 432-6946

Running Title: Refinement by Simulated Annealing

Introduction

X-ray crystallography contributes ever increasingly to an understanding of the structure, function, and control of biological macromolecules. Over the last decade, developments in molecular biology and X-ray diffraction data collection have allowed nearly exponential growth of macromolecular crystallographic studies. The analysis of diffraction data from these studies generally requires sophisticated computational procedures including methods of phasing, density modification, chain tracing, refinement, and structure validation. Many of these procedures can be formulated as chemically–constrained or restrained non–linear optimization of a target function, which usually measures the agreement between observed diffraction data and data computed from a model. This target function normally depends on several parameters such as structure factor phases, scale factors between structure factors, or atomic coordinates.

Here we focus on crystallographic refinement, a technique aimed at optimizing the agreement of an atomic model with both observed diffraction data and chemical restraints. Optimization problems in macromolecular crystallography generally suffer from there being multiple minima, which arise largely from the high dimensionality of the parameter space (typically at least three times the number of atoms in the model). The many local minima of the target function tend to defeat gradient–descent optimization techniques such as conjugate gradient or least-squares methods [1]. These methods are simply not capable of shifting the atomic coordinates enough to correct errors in the initial model.

This limited radius of convergence arises not only from the high dimensionality of the parameter space, but also from what is known as the crystallographic "phase problem" [2]. With monochromatic diffraction experiments on single crystals one can measure the amplitudes of the reflections, but not the phases. The phases, however, are required to compute electron density maps, which are obtained by Fourier transformation of the structure factor described by a complex number for each reflection. Phases for new crystal structures are usually obtained from experimental methods such as multiple isomorphous replacement [3]. However, electron density maps computed from a combination of native crystal amplitudes and multiple isomorphous replacement phases are sometimes insufficiently accurate to allow a complete and unambiguous tracing of the macromolecule. Furthermore, electron density maps for macromolecules are usually obtained at lower than atomic resolution and are therefore prone to human error upon interpretation. A different problem arises when structures are solved by molecular replacement, [4, 5] which uses a similar structure as a search model. In this case the resulting electron density maps can be severely "model–biased", that is, they seem to confirm the existence of the search model without providing clear evidence of actual differences between it and the true crystal structure. In either case, initial atomic models usually require extensive refinement.

This review addresses the common case in which experimental phases are either unavailable or inaccurate. In the unusual case that very good experimental phases are available, refinement is much more straightforward [6]. Experimental phase information tends to increase the degree to which the global minimum of the target function can be distinguished from local

minima. Its omission from the refinement process exacerbates the multiple minima problem to a point that gradient descent methods have little chance of finding the global minimum (Rice & Brunger, in preparation).

Simulated annealing [7, 8, 9] is an optimization technique particularly well suited to the multiple–minima characteristic of crystallographic refinement. Unlike gradient–descent methods, simulated annealing can overcome barriers between minima and thus can explore a greater volume of the parameter space to find "deeper" minima. Following its introduction in 1987 [10], crystallographic refinement by simulated annealing (often referred to as molecular dynamics refinement) was quickly accepted in the crystallographic community because it significantly reduced the amount of human labor required to determine a crystal structure. In fact, more than 75% of all crystal structures published during the past three years were refined by this method [11, 12, 13]. This review summarizes the theory, applications, and recent developments of crystallographic refinement by simulated annealing.

Crystallographic Refinement

Before one attempts to understand the chemistry of the crystallized macromolecule, one has to correct any errors in the initial atomic model. Crystallographic refinement can correct some of the errors. Crystallographic refinement can be formulated as a search for the global minimum of the target function [14]

$$E = E_{\text{chem}} + w_{\text{xray}} E_{\text{xray}}. \tag{1}$$

E_{chem} comprises empirical information about chemical interactions; it is a function of all atomic positions, describing covalent (bond lengths, bond angles, torsion angles, chiral centers, and planarity of aromatic rings) and non-covalent (Van der Waals, hydrogen bonding, and electrostatic) interactions. E_{xray} describes the difference between observed and calculated diffraction data, and w_{xray} is a weight chosen to balance the forces arising from each term. Several algorithms have been developed to minimize E, including least–squares optimization [15, 16, 17], conjugate gradient minimization [14, 18], and simulated annealing refinement [10].

The crystallographic residual E_{xray}

The most common form of E_{xray} consists of the crystallographic residual, defined as the sum over the squared differences between the observed ($|\mathbf{F}_{\text{obs}}(\mathbf{h})|$) and calculated ($|\mathbf{F}_{\text{calc}}(\mathbf{h})|$) structure factor amplitudes:

$$E_{\text{xray}} = \sum_{\mathbf{h}} (|\mathbf{F}_{\text{obs}}(\mathbf{h})| - k|\mathbf{F}_{\text{calc}}(\mathbf{h})|)^2 \tag{2}$$

where $\mathbf{h} = (h, k, l)$ are the indices of the reciprocal lattice points of the crystal. The scale factor k is usually obtained by minimization of Eq. 2. This can be accomplished analytically by setting it to the value that makes the derivative of E_{xray} with respect to k equal to zero. The structure factor of the atomic model is given by

$$\mathbf{F}_{\text{calc}}(\mathbf{h}) = \sum_s \sum_i q_i f_i(\mathbf{h}) \ \exp(-B_i(\mathcal{F}^* \cdot \mathbf{h})^2/4) \ \exp(2\pi i \mathbf{h} \cdot (\mathcal{O}_s \cdot \mathcal{F} \cdot \mathbf{r}_i + \mathbf{t}_s)). \tag{3}$$

The first sum extends over all space group symmetry operators ($\mathcal{O}_s$, $\mathbf{t}_s$) composed of a rotation matrix $\mathcal{O}_s$ and a translation vector $\mathbf{t}_s$. The second

sum extends over all unique atoms i of the system. The quantity $\mathbf{r}_i$ denotes the orthogonal coordinates of atom i in Å. $\mathcal{F}$ is the 3×3 matrix that converts orthogonal (Å) coordinates into fractional coordinates; $\mathcal{F}^*$ is its transpose. B_i, q_i are respectively the atomic temperature factor and occupancy for atom i. The atomic form factors $f_i(\mathbf{h})$ are typically approximated by an expression consisting of several Gaussians and a constant [19]:

$$f_i(\mathbf{h}) = \sum_k a_{ki} \exp(-b_{ki}(\mathcal{F}^* \cdot \mathbf{h})^2/4) + a_{0i}. \tag{4}$$

The structure factor expression given by Eq. 3 is too computation intensive for practical purposes. Approximations are usually made to make crystallographic refinement feasible. One such approximation consists of computing $\mathbf{F}_{\text{calc}}(\mathbf{h})$ by numerical evaluation of the atomic electron density onto a finite grid, followed by Fast Fourier transformation of the electron density. This speeds up the calculation by at least an order of magnitude [20, 21]. Another approximation applied to the minimization process itself, keeps the first derivatives of E_{xray} constant during the refinement process until any atom has moved by more than a specified small distance from the position at which the derivatives were last computed [22].

The standard crystallographic residual (Eq. 2) incorporates information about the amplitudes of the observed reflections only. However, a penalty term ("phase restraints") [23], based on the difference between experimental phases and those calculated from the model, can be added to the residual:

$$E_{\text{xray}} = \sum_{\mathbf{h}} (|\mathbf{F}_{\text{obs}}(\mathbf{h})| - k|\mathbf{F}_{\text{calc}}(\mathbf{h})|)^2 + w_p \sum_{\mathbf{h}} f(\phi_{\text{obs}}(\mathbf{h}) - \phi_{\text{calc}}(\mathbf{h})). \tag{5}$$

Here w_p is the weight given to the phase restraint, and f is a square–well function with a width equal to the arccosine of the figure of merit (m(**h**)) for each reflection. Another possible form of $E_{\rm xray}$ which we call the "vector residual" does not use the amplitude residual at all but instead simultaneously restrains the real (A) and imaginary (B) parts of the structure factor [24]. It has the form

$$E_{\rm xray} = \sum_{\mathbf{h}} m(\mathbf{h}) \left[(A_{\rm obs}(\mathbf{h}) - kA_{\rm calc}(\mathbf{h}))^2 + (B_{\rm obs}(\mathbf{h}) - kB_{\rm calc}(\mathbf{h}))^2 \right]. \quad (6)$$

The chemical term $E_{\rm chem}$

A possible choice of $E_{\rm chem}$ is an empirical potential–energy function [25, 26, 27, 28, 29, 30]

$$\begin{aligned} E_{\rm chem} \;=\; & \sum_{\rm bonds} k_b (r - r_0)^2 + \sum_{\rm angles} k_\theta (\theta - \theta_0)^2 \\ & + \sum_{\rm dihedrals} k_\phi \cos(n\phi + d) + \sum_{\rm chiral,planar} k_\omega (\omega - \omega_0)^2 \\ & + \sum_{\rm atom-pairs} (ar^{-12} + br^{-6} + cr^{-1}) \end{aligned} \quad (7)$$

Empirical energy functions were originally developed for energy–minimization and molecular–dynamics studies of macromolecular structure and function (see [31], for an introduction). The parameters of the empirical potential energy $E_{\rm chem}$ are inferred from experimental as well as theoretical investigations, in particular, vibrational spectroscopy and small-molecule crystallography [25, 26, 27, 28, 29, 30].

Since these energy functions were designed for another purpose, it is not surprising that they require some modification for use in crystallographic refinement. For example, empirical energy functions must be ex-

tended to simulate contacts between molecules related by crystallographic or non–crystallographic symmetry [22, 32]. Empirical energy functions also behave poorly at the high simulation temperatures characteristic of simulated annealing. They must also be modified to cope with the addition of experimental restraints (E_{xray}). To prevent distortions of aromatic rings, peptide bonds, and chiral centers, certain energy constants k_ϕ, k_ω in Eq. 7 often need to be increased [23]. Furthermore, the energy constant k_ϕ for the proline ω angle can be decreased to enable *cis* to *trans* isomerizations. (However, experience has shown [32] that this constant should be set to its original value during the final stages of refinement in order to obtain acceptable geometry about these peptide bonds.) Finally, since bulk solvent is usually omitted from refinement, the charged groups of Asp, Glu, Arg and Lys residues have to be screened in order to avoid formation of artificial interactions with backbone atoms. This can be accomplished either by setting the charges to zero [33, 34].

Apart from the modifications discussed above, crystallographic refinement is not very sensitive to the accuracy of the empirical energy function. Thus, the electrostatic term in Eq. 7 is sometimes purposely omitted to avoid possible bias. Furthermore, one can use a "geometric" energy function consisting of terms for covalent bonds, bond angles, chirality, planarity, and nonbonded repulsion where the corresponding parameters are derived from equilibrium geometry and root–mean–square (r.m.s.) deviations of bond lengths and angles observed in a small-molecule data base [36]. The differences between a geometric energy function and an empirical energy function mainly affect regions that are not well determined by the experimental information. Little difference is observed for well-defined

structures. For instance, the r.m.s. difference for backbone atoms between a structure of crambin refined at 2 Å resolution by PROLSQ [16], a program which effectively uses a geometric energy function, and the same structure refined by conjugate gradient minimization using X-PLOR [37] was only 0.05 Å [22]. Comparison of DNA structures refined by different programs (NUCLSQ, TNT, and X-PLOR) and different parameter sets showed no significant differences within the estimated error of the atomic positions [35].

Additional restraints and constraints

Additional constraints or restraints may be used to improve the ratio of observables to parameters. For example, atoms can be grouped so that they move as rigid bodies during refinement, or bond lengths and bond angles can be kept fixed [15, 38, 39]. The existence of non–crystallographic symmetry in a crystal can be used to average over equivalent molecules and thereby to reduce noise in the data. This is especially useful for virus structures: non-crystallographic symmetry can be used to "overdetermine" the problem, assisting the primary phasing and the subsequent refinement [40, 41, 32].

Weighting

The weight w_{xray} (Eq. 1) balances the forces arising from E_{xray} and E_{chem}. The choice of w_{xray} can be critical: if w_{xray} is too large, the refined structure will show unphysical deviations from ideal geometry; if w_{xray} is too small,

the refined structure will not satisfy the diffraction data. Jack and Levitt [14] proposed that w_{xray} be chosen so that the gradients of E_{chem} and E_{xray} have the same magnitude *for the current structure*. This approach implies that w_{xray} must be readjusted frequently during the course of the refinement. Brunger *et al.* [22] developed an empirical procedure for obtaining a value for w_{xray} that can be kept constant throughout the refinement. It consists of first performing a short molecular dynamics simulation with w_{xray} set to zero, then calculating the final r.m.s. gradient due to the empirical energy term E_{chem} alone. Next one calculates the gradient due to the experimental restraints E_{xray} alone, and chooses w_{xray} to balance the two. A recent correction to this procedure is to divide the resulting w_{xray} by two; this produces optimal phase accuracy as judged by the free R value (Brunger, unpublished data).

Simulated Annealing Refinement

Annealing denotes a physical process wherein a solid is heated until all particles randomly arrange themselves in a viscous liquid phase, and then it is cooled slowly so that all particles arrange themselves in the lowest energy state. By formally defining the target E (Eq. 1) to be the equivalent of the potential energy of the system, one can simulate the annealing process [7]. Simulated annealing is an approximation algorithm: there is no guarantee that it will find the global minimum (except in the asymptotic limit of an infinite search) [8]. Compared to gradient descent methods where search directions must follow the gradient, simulated annealing achieves more optimal solutions by allowing motion against the gradient [7]. The likelihood

of counter-gradient motion is determined by a control parameter referred to as "temperature": the higher the temperature the more likely the optimization will overcome barriers. It should be noted that the simulated annealing temperature normally has no physical meaning and merely determines the likelihood of overcoming barriers of the target function.

The simulated annealing algorithm requires a generation mechanism to create a Boltzmann distribution at a given temperature T

$$B(q_1, \ldots, q_i) = \exp(\frac{-E(q_1, \ldots, q_i)}{k_b T}) \tag{8}$$

where E is given by Eq. 1, k_b is the Boltzmann constant, and $q_1, \ldots, q_i$ are adjustable parameters, such as the coordinates of the atoms. Simulated annealing also requires an annealing schedule, that is, a sequence of temperatures $T_1 \geq T_2 \geq \cdots \geq T_l$ at which the Boltzmann distribution is computed. Implementations of the generation mechanism differ in the way they generate a transition or "move" from one set of parameters to another which is consistent with the Boltzmann distribution at given temperature. The two most widely used generation mechanisms are Metropolis Monte Carlo [45] and molecular dynamics [46] simulations. Metropolis Monte Carlo can be applied to both discrete and continuous optimization problems, but molecular dynamics is restricted to continuous problems.

Monte Carlo

The Metropolis Monte Carlo algorithm [45] simulates the evolution to thermal equilibrium of a solid for a fixed value of the temperature T. Given the current state of system, characterized by the parameters q_i of the system,

a "move" is applied by a shift of a randomly chosen parameter q_i. If the energy after the move is less than the energy before, i.e. if $\Delta E < 0$, the move is accepted and the process continues from the new state. If, on the other hand, $\Delta E \geq 0$, then the move may still be accepted with probability

$$P = \exp(-\frac{\Delta E}{k_b T}) \tag{9}$$

where k_b is Boltzmann's constant. Specifically, if P is greater than a random number between 0 and 1 then the move is accepted. In the limiting case of $T = 0$, Monte Carlo is equivalent to a gradient descent method; the only moves allowed are the ones that lower the target function until a local minimum is reached. At a finite temperature, however, Monte Carlo allows uphill moves and hence allowing for crossing barriers between local minima.

The advantage of the Metropolis Monte Carlo algorithm is its simplicity. A particularly troublesome aspect concerns the efficient choice of the parameter shifts that define the Monte Carlo move. Ideally, this choice should in some way reflect the topology of the search space as characterized by the variables q_i [8]. In the case of a monoatomic liquid or gas, for example, the coordinates of the atoms of the gas are essentially uncoupled so that the coordinate shifts can be chosen in random directions. In the case of a covalently connected macromolecule, however, random shifts of atomic coordinates have a high rejection rate: they immediately violate geometric restrictions such as bond lengths and bond angles. This problem can be alleviated in principle by carrying out the Monte Carlo simulation in a suitably chosen set of internal coordinates such as torsions about bonds, or normal modes of vibration, or by relaxing the strained coordinates through minimization [47, 48, 49].

Cartesian molecular dynamics

A suitably chosen set of continuous (smoothly varying) parameters q_i can be viewed as generalized coordinates that are propagated in time by the Hamilton equations of motion [50]

$$\frac{\partial H(p,q)}{\partial p_i} = \frac{dq_i}{dt} \qquad (10)$$
$$\frac{\partial H(p,q)}{\partial q_i} = -\frac{dp_i}{dt}.$$

Here H(p,q) is the Hamiltonian (the sum of the potential and kinetic energy) of the system and p_i are the generalized momenta conjugate to q_i. If the generalized coordinates represent the atomic coordinates of a molecular system, this approach is referred to as molecular dynamics [46]. If one makes the assumption that the resulting trajectories cover phase space (or more specifically, are ergodic) then they generate a statistical mechanical ensemble [51].

Molecular dynamics can be coupled to a heat bath (see below) so that the resulting ensemble asymptotically approaches that generated by the Metropolis Monte Carlo acceptance criterion (Eq. 9). Thus, molecular dynamics and Monte Carlo are equivalent for the purpose of simulated annealing, although in practice one implementation may be more efficient than the other. Recent comparative work (Adams, Rice, & Brunger, in preparation) has shown the molecular–dynamics implementation of crystallographic refinement by simulated annealing to be more efficient than the Monte Carlo one.

In the special case that the generalized coordinates q_i represent the Cartesian coordinates of n point masses and, furthermore, that momenta

can be separated from coordinates in the Hamiltonian H, the Hamilton equations of motion reduce to the more familiar Newton's second law:

$$m_i \frac{\partial^2 \mathbf{r}_i}{\partial t^2} = -\nabla_i E = \frac{\mathbf{F}_i(\mathbf{r})}{m_i}. \tag{11}$$

The quantities m_i and $\mathbf{r}_i$ are respectively the mass and coordinates of atom i, $\mathbf{F}_i$ is the force acting on atom i, and E is the potential energy. In the context of simulated annealing, E denotes the target function being optimized (Eq. 1), which contains "physical" energies such as covalent and nonbonded energy terms as well as "non-physical" energies that correlate observed and calculated diffraction data. The solution of the partial differential equations (Eq. 11) is normally achieved numerically using finite-difference methods [46]. Initial velocities are usually assigned from a Maxwell distribution at the appropriate temperature.

Torsion angle molecular dynamics

Although Cartesian molecular dynamics places restraints on bond lengths and bond angles, one might want to implement these restrictions as holonomic constraints, i.e., fixed bond lengths and bond angles. This is supported by the observation that the deviations from ideal bond lengths and bond angles are usually small in X-ray crystal structures. There are essentially two possible approaches to solve Newton's equations (Eq. 11) with holonomic constraints. The first involves a switch from Cartesian coordinates $\mathbf{r}_i$ to generalized internal coordinates $\mathbf{q}_i$. Having thus redefined the system, one would solve equations of motion for the generalized coordinates analogous to the Cartesian ones. This formulation has the disadvantage

that it is difficult (but not impossible) to calculate the generalized gradients. Since the gradients are functions of the generalized coordinates only, however, conventional finite-difference integration schemes [46] can be used. A second possible approach is to retain the Cartesian–coordinate formulation so that the gradient calculation remains relatively straightforward and topology independent [39]. In this formulation, however, the expression for the acceleration becomes a more complicated function of positions *and* velocities:

$$\mathbf{a}(\mathbf{r}, \dot{\mathbf{r}}) = \mathbf{M}^{-1}(\mathbf{r})\mathbf{Q}(\mathbf{r}, \dot{\mathbf{r}}) \tag{12}$$

where $\mathbf{a}$ represents the system acceleration vector, and $\mathbf{M}$ and $\mathbf{Q}$ denote the (6×6) system inertia matrix and (6×1) generalized force vector, respectively. This does not present insurmountable difficulties, but instead requires different integration schemes such as a fourth order Runge Kutta integration scheme [52].

The equations of motion for constrained dynamics in this formulation are derived in complete generality by Bae and Haug [53, 54]. We have also produced a slightly simpler derivation specific for fixed bond lengths and bond angles [39]. What follows is a simple sketch of this one particular implementation of molecular dynamics with holonomic constraints.

Consider two bodies, i and j, connected by a bond of fixed length $|\mathbf{h}_{ij}|$. Assuming that the only allowable relative motion between the two bodies is a rotation about $\mathbf{h}_{ij}$, let $\mathbf{r}_i$ and $\mathbf{r}_j$ locate (with respect to an arbitrary inertial frame) the center of mass of body i and j respectively. Let $\mathbf{s}_{ij}$ ($\mathbf{s}_{ji}$) locate the endpoint of $\mathbf{h}_{ij}$ on body i (j) with respect to its center of mass. Thus, $\mathbf{s}_{ij}$ is a vector from the center of mass of body i to

the end of $\mathbf{h}_{ij}$. The position of the center of mass of body j with respect to that of body i is simply $\mathbf{r}_{ij} = \mathbf{r}_j - \mathbf{r}_i$. Finally, the scalar q_{ij} measures the relative angle of rotation about the bond $\mathbf{h}_{ij}$ (cf. [39] for more details).

The assumption that the only allowable relative motion between the two bodies is a rotation about the bond connecting them implies a relationship between the angular velocity $\mathbf{w}$ of their respective centers of mass measured in an inertial ("lab") frame:

$$\mathbf{w}_j = \mathbf{w}_i + \hat{\mathbf{h}}_{ij}\dot{q}_{ij}. \tag{13}$$

Here $\dot{q}_{ij}$ denotes the time derivative of the relative angle between the two bodies and $\hat{\mathbf{h}}_{ij} = \frac{\mathbf{h}_{ij}}{|\mathbf{h}_{ij}|}$ is the unit vector along the bond connecting them. The expression for $\mathbf{r}_j$ can be re-written:

$$\begin{aligned} \mathbf{r}_j &= \mathbf{r}_i + \mathbf{r}_{ij} \\ &= \mathbf{r}_i + \mathbf{s}_{ij} + |\mathbf{h}_{ij}|\hat{\mathbf{h}}_{ij} - \mathbf{s}_{ji} \end{aligned} \tag{14}$$

This expression can be differentiated and then rearranged, resulting in an expression for the center of mass velocity of body j in terms of that of body i:

$$\begin{aligned} \dot{\mathbf{r}}_j &= \dot{\mathbf{r}}_i + \dot{\mathbf{s}}_{ij} + |\mathbf{h}_{ij}|\dot{\hat{\mathbf{h}}}_{ij} - \dot{\mathbf{s}}_{ji} \\ &= \dot{\mathbf{r}}_i + \mathbf{w}_i \times \mathbf{s}_{ij} + |\mathbf{h}_{ij}|\mathbf{w}_i \times \hat{\mathbf{h}}_{ij} - \mathbf{w}_j \times \mathbf{s}_{ji} \\ &= \dot{\mathbf{r}}_i - \mathbf{s}_{ij} \times \mathbf{w}_i - |\mathbf{h}_{ij}|\hat{\mathbf{h}}_{ij} \times \mathbf{w}_i + \mathbf{s}_{ji} \times \mathbf{w}_i - \dot{q}_{ij}\hat{\mathbf{h}}_{ij} \times \mathbf{s}_{ji} \\ &= \dot{\mathbf{r}}_i - \mathbf{r}_{ij} \times \mathbf{w}_i - \left(\hat{\mathbf{h}}_{ij} \times \mathbf{s}_{ji}\right)\dot{q}_{ij} \end{aligned} \tag{15}$$

Thus, assuming certain constraints act between atoms or groups of atoms, one can obtain an expression for the velocity of one group in terms of another. This relationship can be differentiated to give a relationship between accelerations, and integrated to give a relationship between positions.

The algorithm is recursive, so the equations of motion for two bodies easily extend to many. In our implementation, atoms are grouped into rigid bodies, allowing only torsion–angle motions between bodies. The connectivity of these bodies defines a tree–like topology for a macromolecule, with one arbitrarily chosen body identified as the base (or root). As with any molecular–dynamics algorithm, the torsion angle one begins with required positions, velocities, and forces for all atoms at the first step. Then center of mass positions, velocities, and forces are computed for each rigid group. Starting at the outer ends of the tree topology, each chain is 'reduced' one body at a time by solving for the relative acceleration between the tip and the directly inner body. Then the tip's inertial properties are mapped, or aggregated, into the inner body's, resulting in a chain that is effectively one link shorter. This process continues until an expression for the acceleration of the base body is obtained. After solving for the base's acceleration (which only requires inversion of a 6×6 matrix), the aggregation of bodies is reversed. The acceleration of the body "outboard" of the base is determined by the base's acceleration and the relative acceleration between the bodies. This outward expansion is continued until the tree has been completely covered [see [39] for more details]. Then a Runge Kutta integration step updates positions and velocities. Finally, new forces are calculated, and the whole process begins anew. The formalism is a general one: several tree–like topologies can be handled, as can closed topological loops such as those formed by disulfide bonds.

Temperature control

Simulated annealing requires the control of the temperature during molecular dynamics. The three most commonly used methods are velocity scaling, Langevin dynamics, and temperature coupling. The current temperature T_{curr} is computed from the kinetic energy ($E_{\text{kin}} = \sum_i^n \frac{1}{2} m_i (\frac{\partial \mathbf{r}_i}{\partial t})^2$) of the molecular dynamics simulation

$$T_{\text{curr}} = \frac{2E_{\text{kin}}}{3nk_b}. \tag{16}$$

Here n is the number of degrees of freedom and k_b is Boltzmann's constant.

Velocity scaling consists of periodic uniform scaling of the velocities $\mathbf{v}_i$, i.e.,

$$\mathbf{v}_i^{\text{new}} = \frac{\partial \mathbf{r}_i}{\partial t} \sqrt{\frac{T}{T_{\text{curr}}}} \tag{17}$$

for all atoms i where T is the target temperature. The numerical integration of the equations of motion needs to be restarted using the new velocities $\mathbf{v}_i^{\text{new}}$ and current coordinates $\mathbf{r}_i$.

Langevin dynamics incorporates the influence of a heat bath into the classical equations of motion,

$$m_i \frac{\partial^2 \mathbf{r}_i}{\partial t^2} = -\nabla_i E_{\text{total}} - m_i \gamma_i \frac{\partial \mathbf{r}_i}{\partial t} + R(t), \tag{18}$$

where γ_i specifies the friction coefficient for atom i and $R(t)$ is a random force. $R(t)$ is assumed to be uncorrelated with the positions and velocities of the atoms. It is described by a Gaussian distribution with mean of zero and variance

$$< R(t)R(t') >= 2m_i \gamma_i kT \delta(t - t') \tag{19}$$

where k is Boltzmann's constant and $\delta(t - t')$ is the Dirac delta function.

The temperature coupling method of Berendsen [55] is related to Langevin dynamics except that it does not use random forces and it applies a temperature dependent scale factor to the friction coefficient:

$$m_i \frac{\partial^2 \mathbf{r}_i}{\partial t^2} = -\nabla_i E^{\text{total}} - m_i \gamma_i \frac{\partial \mathbf{r}_i}{\partial t}(1 - \frac{T}{T_{\text{curr}}}) \tag{20}$$

The second term on the right hand side of Eq. 20 represents positive friction if $T_{\text{curr}} > T$, thus lowering the temperature; it represents negative "friction" if $T_{\text{curr}} < T$, thus increasing the temperature.

Annealing Schedule

The success and efficiency of simulated annealing depends on the choice of the annealing schedule [56], that is, the sequence of numerical values $T_1 \geq T_2 \geq \cdots \geq T_l$ for the temperature. Note that multiplication of the temperature T by a factor s is formally equivalent to scaling the target E by $1/s$. This applies to both the Monte Carlo as well as the molecular dynamics implementation of simulated annealing. This is immediately obvious upon inspection of the Metropolis Monte Carlo acceptance criterion (Eq. 9). For molecular dynamics this can be seen as follows. Let E be scaled by a factor $1/s$ while maintaining a constant temperature during the simulation,

$$m_i \frac{\partial^2 \mathbf{r}_i}{\partial t^2} = -\nabla_i \frac{E}{s} \tag{21}$$

$$E_{\text{kin}} = \sum_i^n \frac{1}{2} m_i (\frac{\partial \mathbf{r}_i}{\partial t})^2 = \text{const.} \tag{22}$$

This is equivalent to

$$m_i \frac{\partial^2 \mathbf{r}_i}{\partial t'^2} = -\nabla_i E \tag{23}$$

$$E'_{\text{kin}} = \sum_{i}^{n} \frac{1}{2} m_i (\frac{\partial \mathbf{r}_i}{\partial t'})^2 = s E_{\text{kin}} \tag{24}$$

with $t' = \frac{t}{\sqrt{s}}$, i.e., the kinetic energy and, thus, the temperature T_{curr} is scaled by s.

The equivalence between temperature control and scaling of E suggests a generalization of simulated annealing schedules where in addition to the overall scaling of E, relative scale factors between or modifications of the components of the target E are introduced, i.e., simulated annealing is carried out with a adjustable target function. In this case, the annealing schedule denotes the sequence of scale factors or modifications of components of E. A particular example of this type of generalized annealing schedule is the use of a "soft" van der Waals potential during high-temperature molecular dynamics followed by a normal van der Waals potential during the cooling stage [39].

Annealing control

The analogy of simulated annealing with the physical annealing of solids can be more formally expressed through a connection to statistical mechanics. Both Monte Carlo and molecular dynamics simulations can create statistical mechanical ensembles [51]. Approximately, at least, one can use a statistical mechanical language to describe the progress of simulated annealing. For example, changes in the degree of the order of the system can be viewed as phase transitions. They can be detected by finding large values of the specific heat c during the simulation,

$$c = \frac{\langle (E(t) - \langle E(t) \rangle)^2 \rangle}{k_b T^2} \tag{25}$$

where the brackets <> denote the mean computed over appropriate intervals of the simulation. It has been suggested [7] that the cooling rate be reduced at phase transitions since the system is in a critical state where fast cooling might trap the system in a meta–stable state. The observed fluctuations in E are relatively small during simulated annealing refinement, however, indicating local conformational changes rather than global phase transitions [33]. Thus, control of the annealing schedule by monitoring c has not yet been attempted and annealing schedules consisting of a pre-defined sequence of temperatures and modifications of E_{chem} are used.

Commonly used annealing schedules

The two early implementations of simulated annealing refinement made use of the equivalent methods of temperature scaling [10] or energy scaling [57]. The influences of the temperature–control method, energy–term weighting, cooling rate, and duration of the heating stage were studied [33], and it was found that the temperature coupling method by Berendsen and co–workers [55] is preferable to velocity scaling since velocity scaling sometimes causes large temperature fluctuations at high temperatures. Temperature coupling also outperformed Langevin dynamics in the context of simulated annealing since the always positive friction of Langevin dynamics tends to slow atomic motions. Slow–cooling protocols (typically 25K temperature decrements every 25 fsec) produced lower R values than faster–cooling protocols. Constant temperature dynamics represents the extreme limit of slow–cooling

annealing with an infinitely long cooling rate. Thus, constant temperature protocols can outform slow–cooling ones [39].

A typical constant–temperature protocol consists of a high–temperature molecular dynamics stage at 5000K over a period of 2–4 psec, followed by a fast cooling stage at 300K over a period of 0.1 psec. The more robust torsion angle molecular dynamics algorithm outlined above allows conformational sampling at much higher temperatures than are possible with conventional unconstrained molecular dynamics. For refinements of α amylase inhibitor at 5–2 Å resolution, torsion angle dynamics at 10,000 K produces better results than at 5,000K. However, more testing is required to establish the generality of this observation at different resolution ranges and data qualities. Thus, at the present stage, a certain amount of experimentation is required to find the optimal annealing schedule and temperature for each specific refinement problem. Choice of temperature is most influenced by model quality and resolution.

Radius of Convergence

A number of realisitic tests on crambin [22], aspartate aminotransferase [23], myohemerythrin [58], phospholipase A2 [34], thermitase complexed with eglin c [57], and immunoglobulin light chain dimers [59] have shown that simulated annealing refinement starting from initial models (obtained by standard crystallographic techniques) produces significantly improved overall R values and geometry compared to those produced by least-squares optimization or conjugate–gradient minimization.

In recent tests [39], arbitrarily "scrambled" models were generated from an initial model of α-amylase inhibitor built using experimental phase information from multiple isomorphous replacement diffraction data [60]. Scrambling of this initial model was obtained by increasingly long molecular dynamics simulations at 600K computed *without* reference to the X-ray data. Errors were thereby distributed throughout the structure and are probably typical of those found in molecular replacement models or in poorly built initial models. In order to compare the power of refinement techniques, a series of these models was refined using two standard ones: conjugate gradient minimization and slow-cooling simulated annealing.

Results are presented in Fig. 1, which depicts the backbone atom r.m.s. coordinate deviations before and after refinement for a number of different refinement methods. A similar graph for a perfect refinement technique would be a straight line along the horizontal axis: regardless of the initial errors, the final model would be in good agreement with the crystal structure. Clearly this is not the case for conjugate gradient minimization, or even for Cartesian simulated annealing, although Cartesian simulated annealing is a more powerful refinement technique than conjugate gradient minimization. For refinements carried out between 5 and 2 Å, slow-cooling simulated annealing can correct backbone atom r.m.s. coordinate deviations of around 1.3 Å.

Constant–temperature torsion–angle refinements (Fig. 1) outperform the slow-cooling Cartesian protocol on average, dramatically so if one only considers the best model from each series. The torsion angle refinements are able to correct backbone atom r.m.s. coordinate deviations of at least 1.65

Å. Clearly, the backbone atom r.m.s. coordinate deviation is only available if one knows the crystal structure in advance. Fig. 2, however, shows the strong correlation between R_{free} [42, 43, 44] and backbone r.m.s. coordinate deviations. Thus in practice R_{free} can be used to identify the best models from a series of refinements (see chapter by Brunger in this volume).

Simulated annealing has made crystallographic refinement more efficient by automatically moving sidechain atoms by more than 2 Å, by changing backbone conformations, or by flipping peptide bonds *without direct human intervention.* Figure 3 shows a representative case where simulated annealing refinement has essentially converged to a manually refined structure of the enzyme aspartate aminotransferase [23]. The imidazole ring of the histidine sidechain has undergone a 90° rotation around the χ_1 bond during simulated annealing refinement. This rotation was accompanied by significant structural changes of the backbone atoms. This resulted in convergence of the refined structure to the manually refined structure. Conjugate gradient minimization could not arrive at an equally good model without rebuilding. Large rigid-body like corrections of up to 10° resulting from simulated annealing refinement were observed by Gros *et al.* [57].

Simulated annealing refinement is most useful when the initial model is relatively crude. Given a well-refined model, it offers little advantage over conventional methods, with the possible exception of providing information about the accuracy and conformational variability of the refined structure [61]. However, when only a crude model is available, simulated annealing refinement is able to reduce significantly the amount of human intervention required. The initial model can be as crude as one that is obtained by

automatic building based on C^{α} positions alone [62].

In spite of the success of simulated annealing refinement, the importance of manual inspection of the electron density maps after simulated annealing refinement cannot be over-emphasized. Manual inspection is essential for the placement of surface sidechains and solvent molecules, for example, and for checking regions of the protein where large deviations from idealized geometry occur. Figure 4 illustrates a problem that occurred during simulated annealing refinement of influenza virus hemagglutinin [32]. A poorly defined tryptophan sidechain moved into strong density belonging to N–linked carbohydrate that was not included in the model used in the first round of simulated annealing refinement (Fig. 4a). Simulated annealing can move atoms far enough to compensate at least partially for missing parts of the model. The model was rebuilt manually in this region, and the missing carbohydrate was added. In subsequent rounds of simulated annealing, proper model geometry and fit to the electron density map was maintained (Fig. 4b).

Simulated annealing refinement can produce R values in the twenties for partially incorrect structures. For example, after refinement of the protease from human immunodeficiency virus HIV-1 a partially incorrect structure [63] produced an R value of 0.25 whereas the correct structure produced a R value of 0.184 [64] with comparable geometry.

Why Does It Work?

The goal of any optimization problem is to find the global minimum of a target function. In the case of crystallographic refinement, one searches for the conformation or conformations of the molecule that best fit the diffraction data at the same time that they maintain reasonable covalent and non-covalent interactions. As the above examples have shown, simulated annealing refinement has a much larger radius of convergence than gradient descent methods. It must therefore be able to find a lower minimum of the target E (Eq. 1) than the local mimimum found by simply moving along the negative gradient of E. Paradoxically, the very reasons that make simulated annealing such a powerful refinement technique (the ability to overcome barriers in the target energy function) would seem to prevent it from working at all. If it crosses barriers so easily, what allows it to stay in the vicinity of the global minimum?

The answer lies in the temperature coupling. By specifying a fixed kinetic energy, the system essentially gains a certain inertia which allows it to cross energy barriers. The target temperature must be low enough, however, to ensure that the system will not "climb out" out from the global minimum if it manages to arrive there. While temperature itself is a global parameter of the system, temperature fluctuations arise principally from local conformational transitions - for example from an amino acid sidechain falling into the correct orientation. These local changes tend to lower the value of the target E, thus increasing the kinetic energy, and hence the temperature, of the system. Once the temperature coupling has removed this excess kinetic energy, the reverse transition is very unlikely, since it

would require a localized increase in kinetic energy where the conformational change occurred in the first place. Temperature coupling maintains a sufficient amount of kinetic energy to allow local conformational corrections, but does not supply enough to allow escape from the global minimum. This explains the directionality of simulated annealing refinement, i.e., on average the agreement with the data will improve rather get worse. It also explains the occurrence of small spikes in E during the simulated annealing process [33].

If the temperature of the simulated annealing refinement is too high, numerical instabilities can result in unreasonably large conformational changes. By suppressing high-frequency bond vibrations, torsion angle dynamics has significantly reduced the potential for this to happen. In fact, one may now use much higher temperatures than previously possible with the Cartesian molecular dynamics implementation [39].

Refinements at 3–4 Å Resolution

There are two related issues concerning initial models and crystallographic refinements: convergence and determinacy. For example, it is possible to have high resolution data but a very poor initial model, in which case the refinement is well-determined but may encounter problems of convergence, or searching. It is equally possible to have an excellent starting model but only low to medium resolution data. Refinement under these conditions does not have a severe search problem in that the initial model lies close to the correct one, but it is hampered by the fact that the correct answer

may not be well determined by the limited experimental data. The question therefore arises: when is it appropriate to use torsion angle refinement, and when do Cartesian methods suffice?

In order to address this question, a series of refinements were carried out at progressively lower resolution (Fig. 5). The crystal structure coordinates of the α-amylase inhibitor were subjected to ten constant temperature torsion angle refinements and ten constant temperature Cartesian molecular dynamics refinements at resolutions of 5-2.5 Å, 5-3.0 Å, 5-3.5 Å, 5-4.0 Å, 5-4.5 Å. For the refinements at 5-2.5 Å resolution, the two methods yield more or less equivalent results, but at resolutions below 3 Å the torsion angle method shows considerable advantage. Thus for good initial models, Cartesian methods are sufficient if data better than 3 Å resolution are available. Torsion angle dynamics should be used otherwise.

The free R value shows a high correlation with the model's accuracy as assessed by the r.m.s. difference and phase difference between the low–resolution refined model and the 2 Å crystal structure (Fig. 5) except for the refinement at 5–4.5 Å resolution where the differences in free R values are very small. However, in the latter case the free R value has nearly reached the limit for a random distribution of atoms in non–centric spacegroups (57%), indicating divergence of refinement at 4.5 Å resolution.

The poorer performance of Cartesian molecular dynamics below 3 Å resolution is a consequence of the under–determinacy of refinement at that resolution (the number of reflections is half the number of coordinates). Restricting refinement to torsion angles makes the search more efficient and it improves the representation of the model at low to medium resolution. For

example, at 3 Å resolution, torsion angle dynamics is superior to Cartesian dynamics. If the torsion dynamics is followed by a very brief Cartesian slow-cooling stage starting at low temperature, the performance is even better at resolutions around 3 Å (not shown). Thus, torsion angle dynamics acheives a better search, but once the structure has reached the vicinity of the global minimum, adjustment of all parameters (including bond lengths and bond angles) may be beneficial, even at 3 Å resolution.

Simulated–Annealing Omit Maps

Simulated annealing refinement is usually unable to correct very large errors in the atomic model or to correct for missing parts of the structure. The atomic model needs to be corrected by inspection of a difference electron density map. In order to improve the quality and resolution of the difference electron density map, the observed phases are often replaced or combined with calculated phases as soon as an initial atomic model has been built. These combined electron–density maps are then used to improve and to refine the atomic model. The inclusion of calculated phase information brings with it the danger of biasing the refinement process towards the current atomic model. This model bias can obscure the detection of errors in atomic models if sufficient experimental phase information is unavailable. In fact during the past decade several cases of incorrect or partly incorrect atomic models have been reported where model bias may have played a role [66].

Difference electron density maps phased with simulated–annealing

refined structures often show more details of the correct chain trace [23]. However, the omission of some atoms from the computation of a difference electron density map does not fully remove phase bias towards those atoms if they were included in the preceeding refinement. More precisely, small re-arrangements of the included atoms can bias the phases towards the omitted atoms [67]. Thus, the structure needs to be re-refined with the questionable region omitted before the difference electron density map can be computed. Simulated annealing is a particularly powerful tool for removing model bias [68]. The improved quality of simulated annealing refined omit maps has been used to bootstrap about 50% of missing portions of an initial atomic model of a DNase-Actin complex [69]. It should be noted that this is a rather extreme case for the amount of omitted atoms. Usually, omit maps are computed with about 10% of the atoms omitted.

In general, the improvement of the electron density map achieved in simulated annealing refinement is a consequence of conformational changes distributed throughout the molecule. This is a reflection of the fact that the first derivatives of the crystallographic residual (Eq. 1) with respect to the coordinates of a particular atom depend not only on the coordinates of that atom and its neighbors but also on the coordinates of all other atoms including solvent atoms in the crystal structure.

Refinement with Phase Restraints

As demonstrated throughout, simulated annealing has a large radius of convergence. The use of torsion–angle molecular dynamics combined with

a repeated high-temperature annealing schedule significantly increased the radius of convergence compared to a slow–cooling Cartesian protocol *at relatively high resolution.* However, for refinements at lower resolution (¿ 3Å), no significant extension of the radius of convergence was observed when refining against structure factor amplitudes alone [39]. Convergence at this resolution range can be sparse: the limited resolution drastically reduces the number of reflections (observables) and can result in a severely underdetermined search problem.

This adverse observable to parameter ratio can be improved using experimental phase information, for example phases obtained from multiple isomorphous replacement diffraction data. Use of phase restraints (Eq. 5) improves the radius of convergence somewhat, and the vector residual (Eq.6) shows a significantly increased radius of convergence [39]. Figure 6 summarizes convergence for refinements at 5 to 3Å resolution, again using backbone atom r.m.s. coordinate deviations from the crystal structure as a measure of convergence. As for high resolution refinements, torsion angle refinements consistently outperform slow–cooling Cartesian refinement (Fig. 6). These refinements were performed without cross-validation because the phase accuracy could be assessed by direct comparison with the experimental phases [44]. There is, however, a strong correlation between the R value and backbone atom r.m.s. coordinate deviations. This is not the case in general, since R values for medium resolution refinements performed without phase information do not distinguish as well between good and bad models (Fig. 5b).

Conclusions

Simulated annealing has improved the efficiency of crystallographic refinement significantly. However, simulated annealing refinement alone is still insufficient to refine a crystal structure automatically without human intervention. Thus, crystallographic refinement of macromolecules proceeds in a series of steps, each of which consists of simulated annealing or minimization of E (Eq. 1) followed by manual re–fitting the model to difference electron density maps using interactive computer graphics [62]. During the final stages of refinement, solvent molecules are usually included, and alternate conformations for some atoms or residues in the protein may be introduced.

With currently available computing power, tedious manual adjustments using computer graphics to display and move positions of atoms of the model in the electron density maps can represent the rate–limiting step in the refinement process. Further automation of refinement by judicious combination of reciprocal and real–space refinements should be possible. However, all automation attempts will ultimately have to address the problem of pattern recognition of macromolecular features in noisy electron density maps. The human brain appears to be highly efficient at solving this problem whereas computer algorithms have been rather slow in achieving this ability. Thus, for the near-term future, the main goal should be to eliminate tedious book–keeping and computer graphics-bound intervention by automating all aspects of refinement that do not require significant pattern recognition.

Acknowledgment

We are grateful to Erin Duffy for critical reading of the manuscript. L.M.R. is an HHMI predoctoral fellow. This work was funded in part by a grant from the National Science Foundation (DIR 9021975).

References

[1] W.H. Press, B.P. Flannery, S.A. Teukolosky, and W.T. Vetterling, Numerical Recipes, Cambridge University Press, Cambridge, 1986.

[2] H.A. Hauptman, *Physics Today*, **42** 24–29 (1989).

[3] D.M. Blow and F.H.C. Crick, *Acta Cryst.*, **12** 794–802 (1959).

[4] W. Hoppe, *Acta Cryst.*, **10** 750–751 (1957).

[5] M.G. Rossmann and D.M. Blow, *Acta Cryst.*, **A15** 24–31 (1962).

[6] W.I. Weis, R. Kahn, R. Fourme, K. Drickamer, and W.A. Hendrickson, *Science*, **254** 1608–1615 (1991).

[7] S. Kirkpatrick, C.D. Gelatt, and M.P. Vecchi, Jr., *Science*, **220** 671-680 (1983) .

[8] P.J.M. Laarhoven and E.H.L. Aarts (eds.), Simulated Annealing: Theory and Applications, Dordrecht: D. Reidel Publishing Company, 1987.

[9] M.E. Johnson, *American Journal of Mathematical and Management Science*, **8** 205–450 (1988) .

[10] A.T. Brunger, J. Kuriyan, and M. Karplus, *Science*, **235** 458–460 (1987).

[11] W.A. Hendrickson and K. Wüthrich, Macromolecular Structures 1991, Atomic Structures of Biological Macromolecules Reported During 1990. Current Biology Ltd., London, 1991.

[12] W.A. Hendrickson and K. Wüthrich, Macromolecular Structures 1992, Atomic Structures of Biological Macromolecules Reported During 1991. Current Biology Ltd., London, 1992.

[13] W.A. Hendrickson and K. Wüthrich, Macromolecular Structures 1993, Atomic Structures of Biological Macromolecules Reported During 1992. Current Biology Ltd., London, 1993.

[14] A. Jack and M. Levitt, *Acta Cryst.*, **A34** 931–935 (1978).

[15] J.L. Sussman, S.R. Holbrook, G.M. Church, and S.-H. Kim, *Acta Cryst.*, **A33** 800–804 (1977).

[16] J.H. Konnert and W.A. Hendrickson, *Acta Cryst.*, **A36** 344–349 (1980).

[17] W.A. Hendrickson, *Meth. Enzymol.*, **115** 252–270 (1985).

[18] D.E. Tronrud, L.F. Ten Eyck, and B.W. Matthews, *Acta Cryst.*, **A43** 489–500 (1987).

[19] J. Ibers and W.C. Hamilton (eds.), International Tables for X-ray Crystallography. International Union of Crystallography, The Kynoch Press, Birmingham, 1974.

[20] L.F. Ten Eyck, *Acta Cryst.*, **A29** 183–191 (1973).

[21] A.T. Brunger, *Acta Cryst.*, **A45** 42–50 (1989).

[22] A.T. Brunger, M. Karplus, and G.A. Petsko, *Acta Cryst.*, **A45** 50–61 (1989).

[23] A.T. Brunger, *J. Mol. Biol.*, **203** 803–816 (1988).

[24] E. Arnold and M.G. Rossmann, *Acta Cryst.*, **A44** 270–282 (1988).

[25] S. Lifson and P. Stern, *J. Chem. Phys.*, **77** 4542–4550 (1982).

[26] B.R. Brooks, R.E. Bruccoleri, B.D. Olafson, D.J. States, S. Swaminathan, et al., *J. Comput. Chem.*, **4** 187–217 (1983).

[27] G. Némethy, M.S. Pottie, and H.A. Scheraga, *J. Phys. Chem.*, **87** 1883–1887 (1983).

[28] J. Hermans, H.J.C. Berendsen, W.F. van Gunsteren, and J.P.M. Postma, *Biopolymers*, **23** 1513–1518 (1984).

[29] L. Nilsson and M. Karplus, *J. Comp. Chem.*, **7** 591–616 (1986).

[30] S.J. Weiner, P.A. Kollman, D.T. Nguyen, and D.A. Case, *J. Comp. Chem.*, **7** 230–252 (1986).

[31] M. Karplus and G.A. Petsko, *Nature*, **347** 631–639 (1990).

[32] W.I. Weis, A.T. Brunger, J.J. Skehel, and D.C. Wiley, *J. Mol. Biol.*, **212** 737–761 (1989).

[33] A.T. Brunger, A. Krukowski, and J. Erickson, *Acta Cryst.*, **A46** 585–593 (1990).

[34] M. Fujinaga, P. Gros, and W.F. van Gunsteren, *J. Appl. Cryst.*, **22** 1–8 (1989).

[35] M. Hahn and U. Heinemann, *Acta. Cryst.*, **D5** 468-477 (1993).

[36] R.A. Engh and R. Huber, *Acta Cryst.*, **A47** 392-400 (1991).

[37] A.T. Brunger, X-PLOR, Version 3.1. A System for X-ray Crystallography and NMR. Yale University Press, New Haven, 1992.

[38] R. Diamond, *Acta Cryst.*, **A27** 436-452 (1971).

[39] L.M. Rice and A.T. Brunger, *Proteins: Structure, Function, and Genetics*, **19** 277–290 (1994).

[40] J.N. Champness, A.C. Bloomer, G. Bricogne, P.J.G. Butler, and A. Klug, *Nature*, **259** 20–24 (1976).

[41] M.G. Rossmann, E. Arnold, J.W. Erickson, E.A. Frankenberger, J.P. Griffith, et al., *Nature*, **317** 145–153 (1985).

[42] A.T. Brunger, *Nature*, **355** (1992) 472–474.

[43] A.T. Brunger, *Acta Cryst.*, **D49** (1993) 24–36.

[44] A.T. Brunger, *Meth. Enzym*, this volume.

[45] N. Metropolis, M. Rosenbluth, A. Rosenbluth, A. Teller, and E. Teller, *J. Chem. Phys.*, **21** 1087–1092 (1953).

[46] L. Verlet, *Phys. Rev.*, **159** 98–105 (1967).

[47] M. Saunders, *J. Am. Chem. Soc.*, **109** 3150–3152 (1987).

[48] Z. Li and H.A. Scheraga, *Proc. Natl. Acad. Sci. USA*, **84** 6611–6615 (1987).

[49] R. Abagyan and P. Argos, *J. Mol. Biol.*, **225** 519–532 (1992).

[50] H. Goldstein, Classical Mechanics, 2nd ed., Addison-Wesley Pub. Co., Reading, Massachusetts, 1980.

[51] D.A. McQuarrie, Statistical Mechanics, Harper & Row, New York, 1976.

[52] M. Abramowitz and I. Stegun, Handbook of Mathematical Functions, Applied Mathematics Series, vol. 55, Dover Publications, New York, 1968.

[53] D.-S. Bae and E.J. Haug, *Mech. Struct. & Mach.*, **15** 359–382 (1987).

[54] D.-S. Bae and E.J. Haug, *Mech. Struct. & Mach.*, **15** 481–506 (1988).

[55] H.J.C. Berendsen, J.P.M. Postma, W.F. van Gunsteren, A. DiNola, and J.R. Haak, *J. Chem. Phys.*, **81** 3684–3690 (1984).

[56] D.G. Bounds, *Nature (London)*, **329** 215–219 (1987).

[57] P. Gros, M. Fujinaga, B.W. Dijkstra, K.H. Kalk, and W.G.J. Hol, *Acta Cryst.*, **B45** 488–499 (1989).

[58] J. Kuriyan, A.T. Brunger, M. Karplus, and W.A. Hendrickson, *Acta Cryst.*, **A45** 396–409 (1989).

[59] Z.-B. Xu, C.-H. Chang, and M. Schiffer, *Protein Engineering*, **3** 583–589 (1990).

[60] J.W. Pflugrath, G. Wiegand, R. Huber, and L. Vértesey, *J. Mol. Biol.*, **189** 383-386 (1986).

[61] F.T. Burling and A.T. Brunger, *Israel Journal of Chemistry* **34**. 165–175 (1994).

[62] T.A. Jones, J.-Y. Zou, S.W. Cowan, and M. Kjeldgaard, *Acta Cryst.*, **A47** 110–119 (1991).

[63] M.A. Navia, P.M.D. Fitzgerald, B.M. McKeever, C.-T. Leu, J.C. Heimbach, et al., *Nature*, **37** 615–620 (1989).

[64] A. Wlodawer, M. Miller, M. Jaskólski, B.K. Sathyanarayana, E. Baldwin, et al., *Science*, **245** 616–621 (1989).

[65] A.T. Brunger, *Acta Cryst.* **A46**, 46–57 (1990).

[66] C.I. Brändén and A. Jones, *Nature.*, **343** (1990) 687–689.

[67] R.J. Read, *Acta Cryst.*, **A42** 140–149 (1986).

[68] A. Hodel, S.-H. Kim, and A.T. Brunger, *Acta Cryst.*, **48** 851–859 (1992).

[69] W. Kabsch, H.G. Mannherz, D. Suck, E.F. Pai, and K.C. Holmes, *Nature*, **347** 37–44 (1990).

Figure Captions

Figure 1: Radius of convergence of conjugate–gradient minimization, Cartesian slow–cooling, and torsion–angle simulated annealing. Convergence is measured by the final backbone atom r.m.s. coordinate deviation to the crystal structure. Thin lines show the result from one conjugate gradient minimization (dashed) or one slow-cooling simulated annealing refinement (solid). The thick dot-dashed line shows the average backbone atom r.m.s. coordinate deviation obtained from ten high–temperature torsion–angle refinements at 5000K, and the thick solid line shows the backbone atom r.m.s. coordinate deviation achieved by the torsion angle refinement with the lowest free R value.

Figure 2: Free R value vs. backbone atom r.m.s. coordinate deviation for torsion-angle constant–temperature refinements using α-amylase inhibitor [60] as a test case.

Figure 3: The segment consisting of residues Cys-192 and His-193 of the 2.8 Å resolution structure of a single site mutant of aspartate aminotransferase [23]. Superimposed are the initial structure (dotted lines) obtained by fitting the atomic model to a multiple isomorphous replacement map, the structure obtained after several cycles of rebuilding and restrained least-squares refinement (thick lines), the structure obtained after simulated annealing refinement (thin lines), and the structure obtained after conjugate gradient minimization (dashed lines).

Figure 4: Simulated annealing refinement can move atoms far from their initial positions to compensate for missing model atoms. Residue Trp 222 of influenza virus hemagglutinin, which has weak sidechain density, moved into strong N-linked carbohydrate density in the first round of simulated annealing refinement, before carbohydrate was added to the model. The electron density maps were computed from $(2F_{\rm obs} - F_{\rm calc})$ amplitudes using $F_{\rm calc}$ phases corresponding to the atomic models at 3.0 Å resolution. It shows density corresponding to missing atoms as well as the current model. The electron density maps are displayed as a "chicken wire" which represents the density at a constant level of one standard deviation above the mean. The maps have been averaged about the 3-fold non-crystallographic symmetry axis. (a) Electron density and coordinates after round 1, showing missing density for Trp 222 C^{β}. (b) as in (a), showing properly built N–linked carbohydrate and Trp 222.

Figure 5: Cartesian and torsion angle refinements at low to medium resolution. Averages over ten refinements are shown. The crystal structure of the α-amylase inhibitor was refined against artificially truncated sets of the original diffraction data [60]. (a) Atomic r.m.s. differences and phase differences between the models refined at the specified resolution range and the deposited crystal structure. (b) Free R and R values.

Figure 6: Convergence of medium resolution slow–cooling (starting at 5000K, dashed line) and constant temperature torsion angle (10,000K, solid line) refinements against the vector residual (Eq. 6) at 5–3 Å of increasingly worse models for amylase inhibitor [60]. Convergence is measured by backbone atom r.m.s. coordinate deviations from the crystal structure, taking the best structure from a series of ten independent refinement obtained by using different initial random velocities for simulated annealing. The best models can be identified by a low free R value [39].

Fig.1

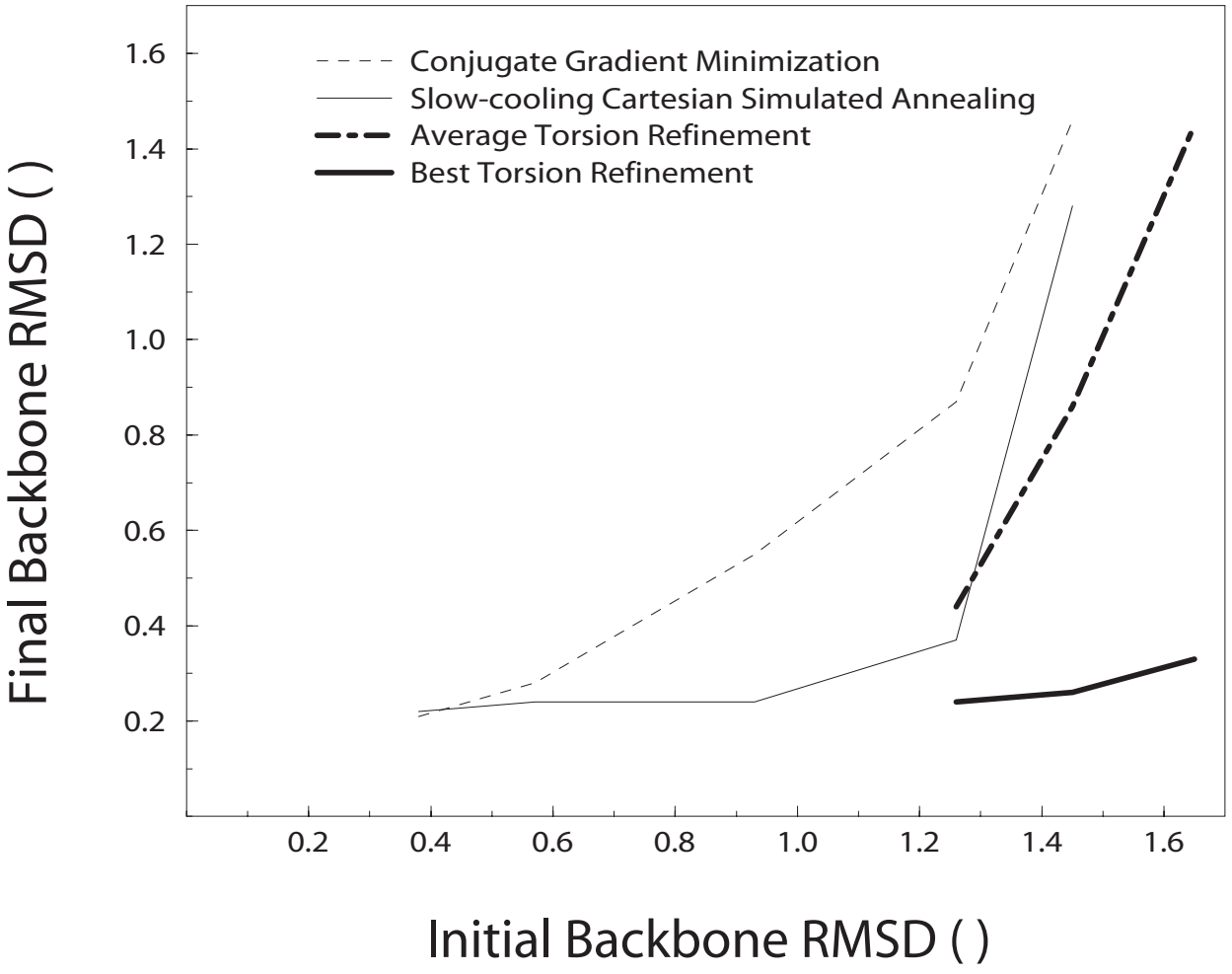
Conjugate Gradient Minimization
Slow-cooling Cartesian Simulated Annealing
Average Torsion Refinement
Best Torsion Refinement
Final Backbone RMSD ( )
Initial Backbone RMSD ( )
0.2
0.4
0.6
0.8
1.0
1.2
1.4
1.6

Fig.2

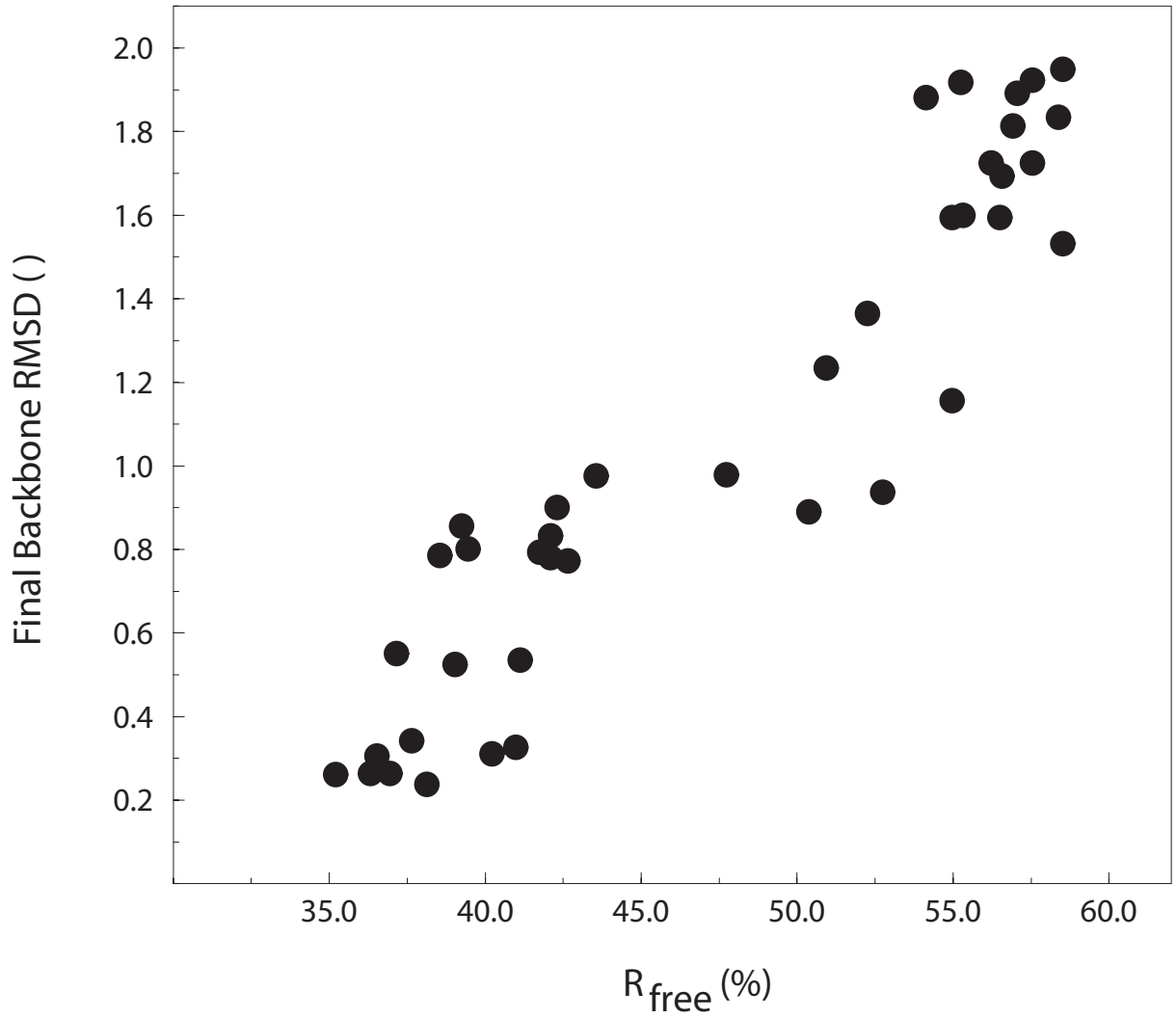
Final Backbone RMSD ( )
2.0
1.8
1.6
1.4
1.2
1.0
0.8
0.6
0.4
0.2
35.0
40.0
45.0
50.0
55.0
60.0
R free (%)

Fig.3

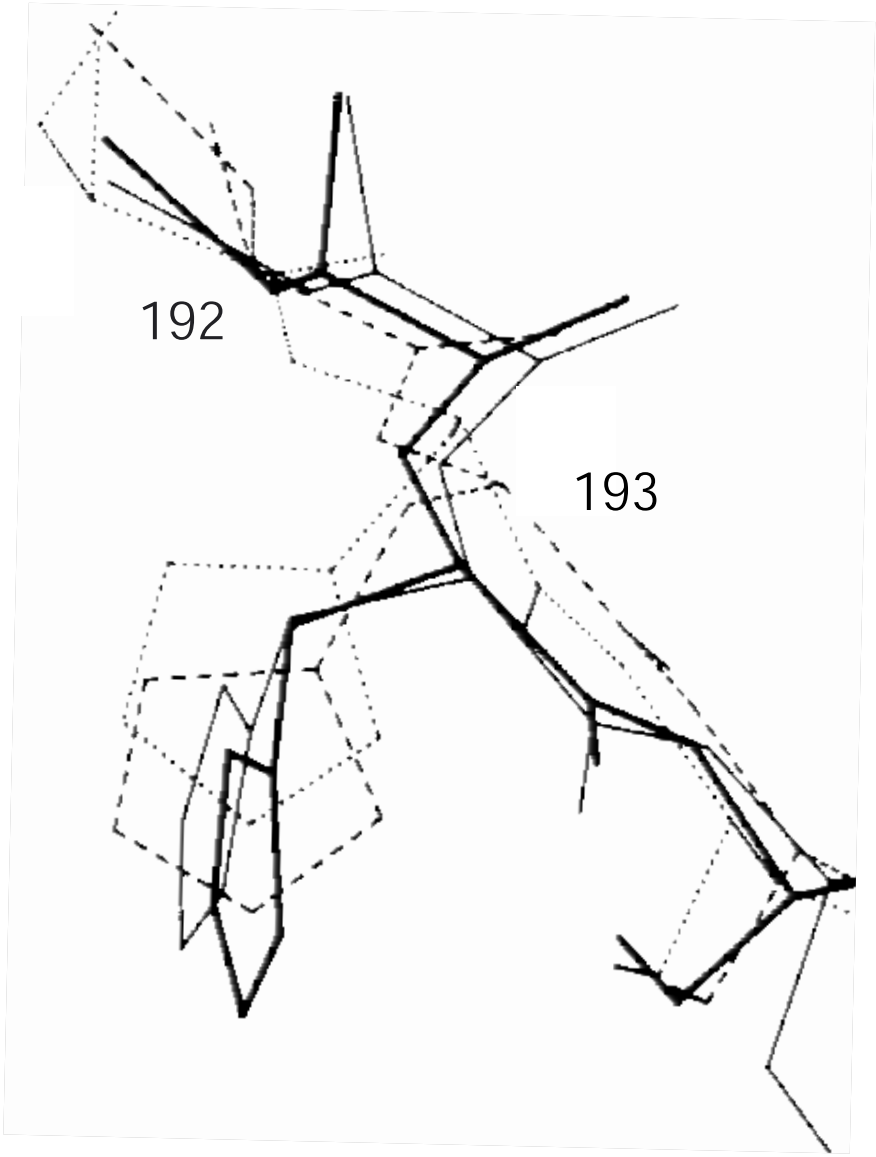

Fig.4

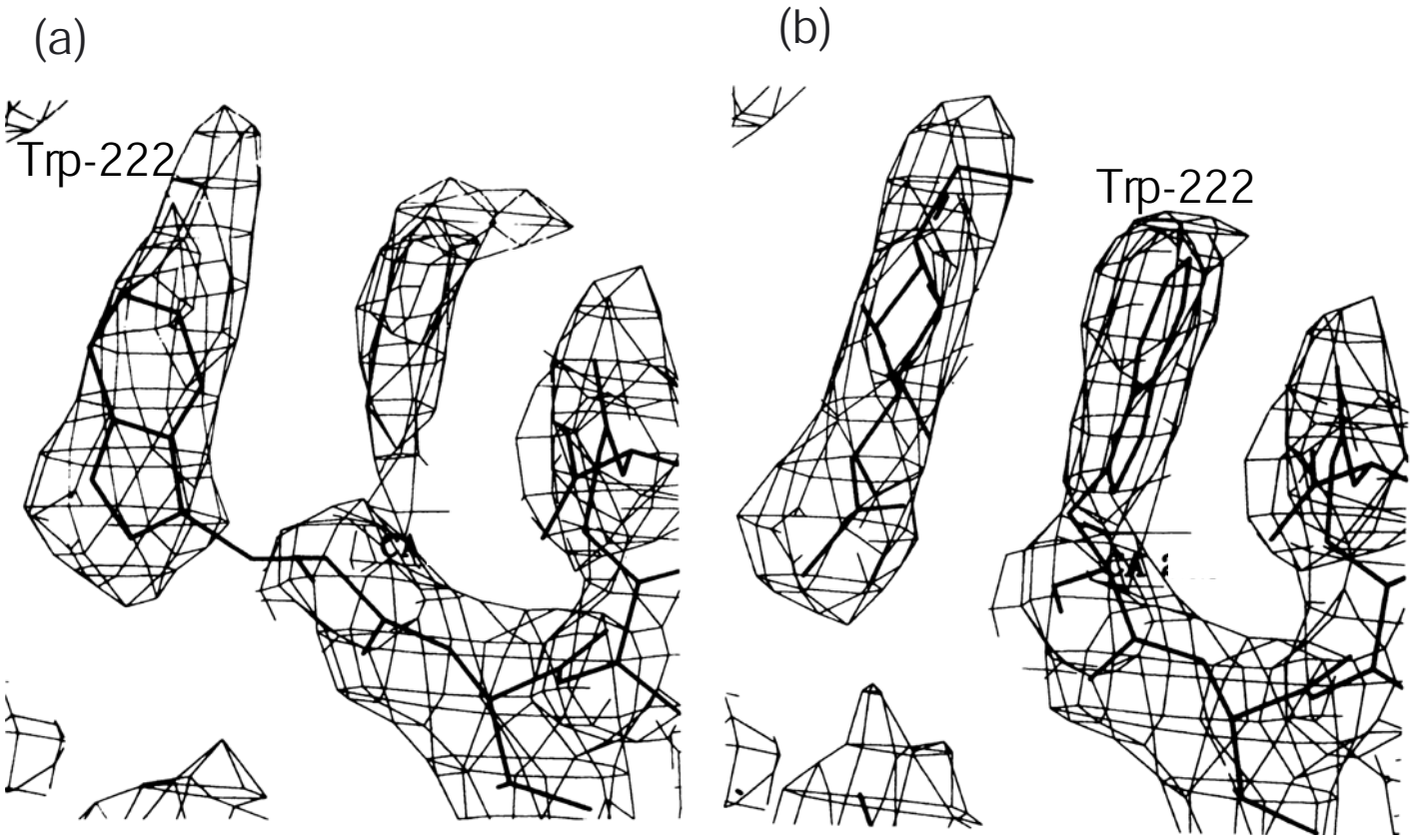

Fig.5

(a)

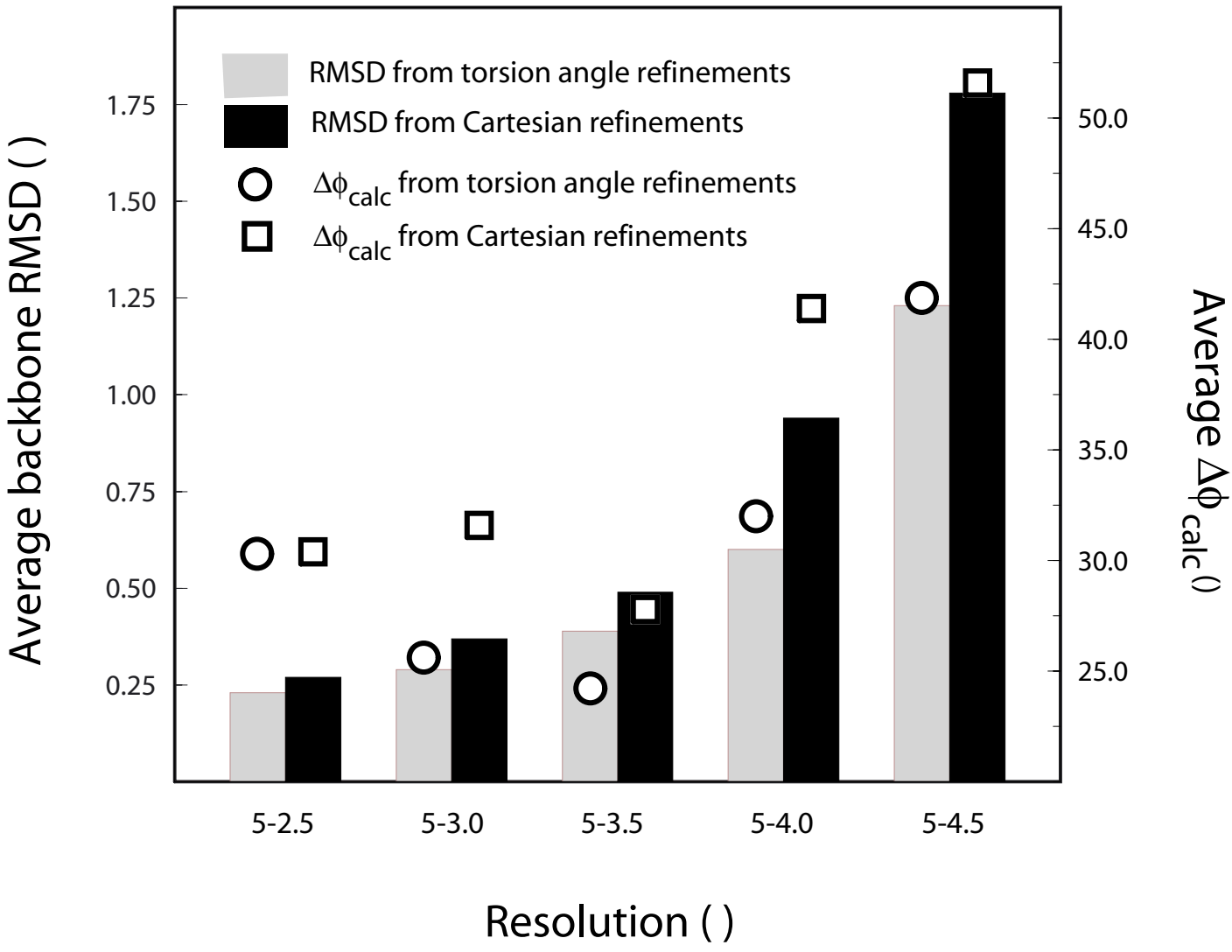
RMSD from torsion angle refinements
RMSD from Cartesian refinements
$\Delta\phi_{calc}$ from torsion angle refinements
$\Delta\phi_{calc}$ from Cartesian refinements
Average backbone RMSD ( )
Average $\Delta\phi_{calc}$ ()
1.75
1.50
1.25
1.00
0.75
0.50
0.25
50.0
45.0
40.0
35.0
30.0
25.0
5-2.5
5-3.0
5-3.5
5-4.0
5-4.5
Resolution ( )

Fig.5

(b)

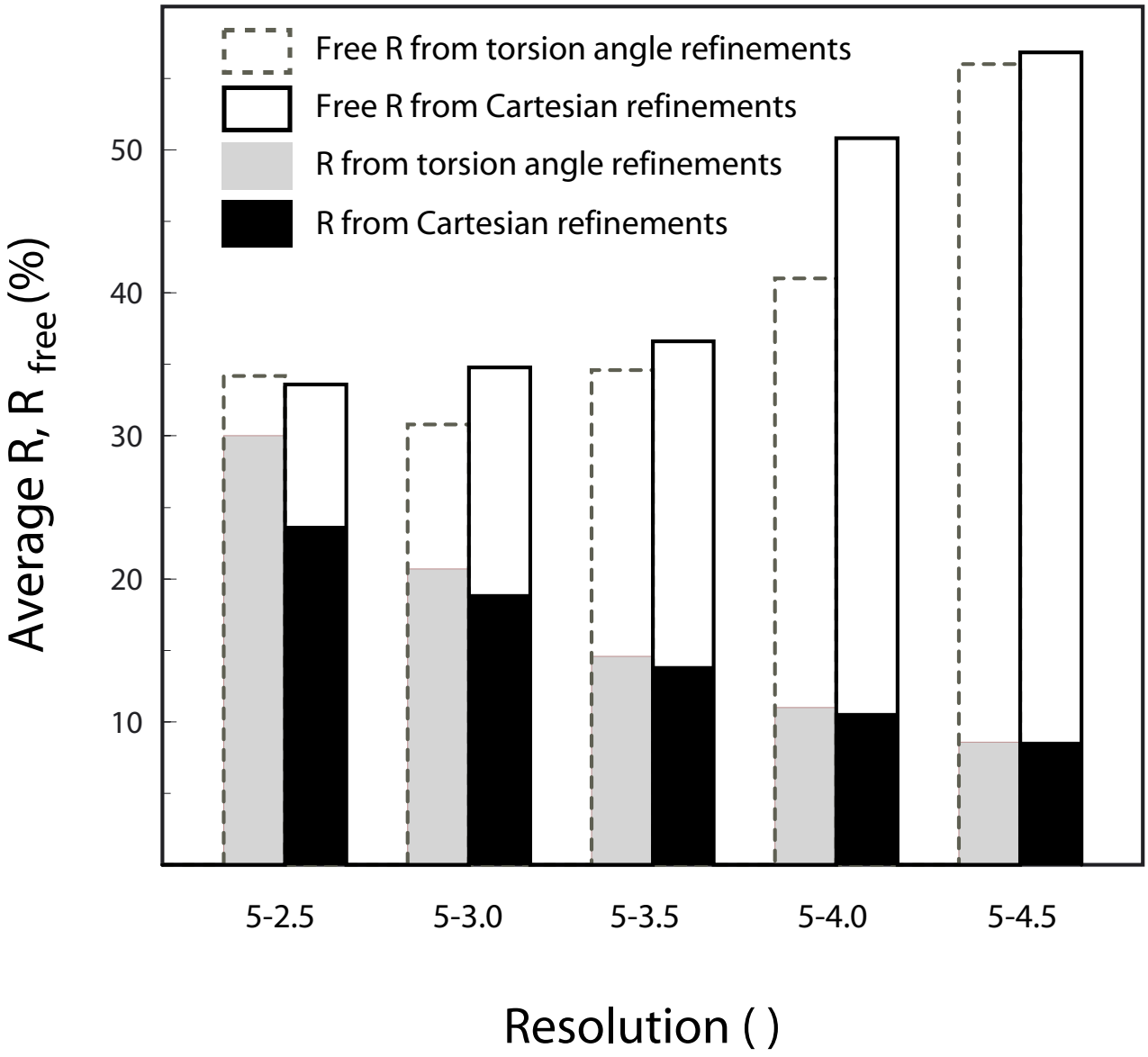
Free R from torsion angle refinements
Free R from Cartesian refinements
R from torsion angle refinements
R from Cartesian refinements
Average R, R free (%)
50
40
30
20
10
5-2.5
5-3.0
5-3.5
5-4.0
5-4.5
Resolution ( )

Fig.6

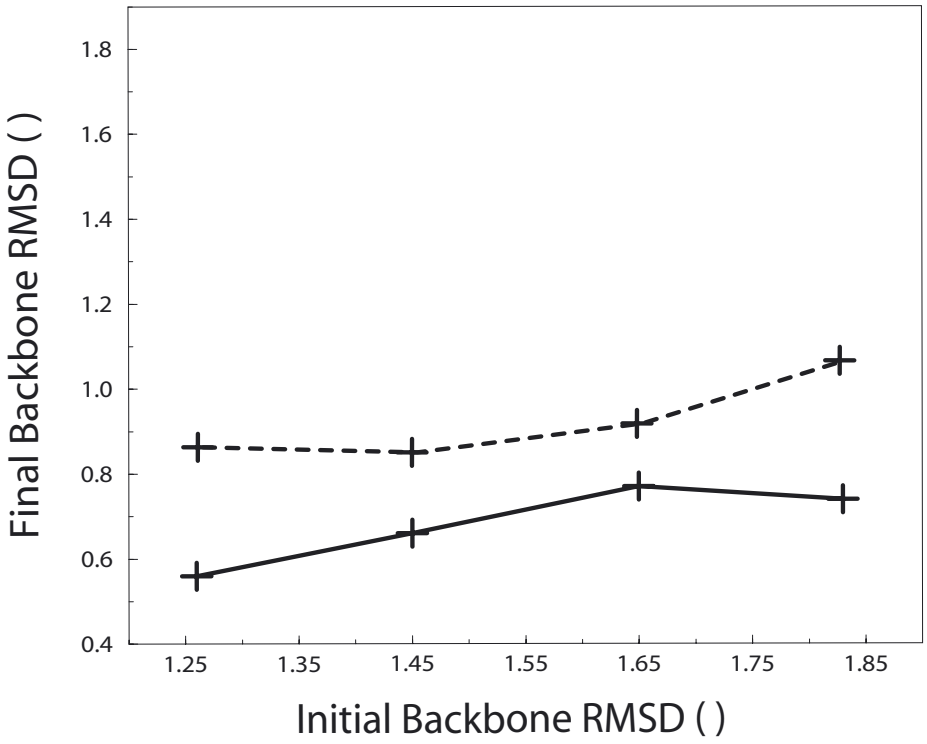
Final Backbone RMSD ( )
1.8
1.6
1.4
1.2
1.0
0.8
0.6
0.4
1.25
1.35
1.45
1.55
1.65
1.75
1.85
Initial Backbone RMSD ( )